Synthesis and Multiscale Evaluation of $LiNbO_3$-Containing Silicate Glass-Ceramics with Efficient Isotropic SHG Response

Hélène Vigouroux, Evelyne Fargin, Sonia Gomez, Bruno Le Garrec, Grigoris Mountrichas, Efstratios Kamitsos, Frédéric Adamietz, Marc Dussauze, and Vincent Rodriguez**

A study of bulk second harmonic generation (SHG) response of lithium niobium silicate glass-ceramics is presented. The observed macroscopic SHG signals have an isotropic 3D nature. To interpret this particular nonlinear optical response, a multiscale approach is used in which clear correlations between structure and optical response are characterized from the sub-micrometer to the millimeter scale. In particular, it is inferred that the radial distribution of the $LiNbO_3$ crystallites in spherulite domains is at the origin of the isotropic bulk second order optical property. It is suggested that spherulitic crystallization in glass-ceramic is a challenging method to elaborate isotropic nonlinear optical properties in inorganic materials.

1. Introduction

Second order optical properties are fundamental for all applications in which electro-optical effects and optical frequency conversions are required. In order to develop micro photonic devices one should be able to structure non linear optical responses at the micrometer scale,[1–8] while optical elements with meter scale dimensions and large damage threshold should be developed for high power laser facilities. For both of these extreme cases of applications, glass ceramics with ferroelectric crystalline phase are of great interest.[9,10]

Within the family of ferroelectric crystalline phases, lithium niobate ($LiNbO_3$) is widely used as single crystal in micro integrated optical technology for its large electro-optic coefficients and in laser development for frequency conversions.[1–5] In glass ceramics, the growth of lithium niobate crystalline particles has been also widely studied.[11–15] The classical methodology to fabricate a glass ceramic with appropriate physical properties is based on the optimization of several heat treatments to control first the nucleation and then the growth of the crystalline particles in the glass. By this way, it is possible to promote either surface and/or bulk crystallization and to control the size and dispersion of crystallites.[15–17]

A controlled and efficient bulk second harmonic generation (SHG) response is a key objective in glass ceramic development in order to consider this class of material as potential cheap and reliable optical elements, especially in large scale optical facilities such as high power laser installations. Bulk SHG signals have been observed in several glass ceramics systems such as in $LaBGeO_5$,[18] TiO_2-BaO-B_2O_3 and TiO_2-BaO-SiO_2[19–21] and also chalcogenide and chalcohalide compositions.[22–25] Permanent broad SHG patterns have been observed and attributed either to the lack of coherency of the SH waves generated from two surface crystalline layers and/or to randomly oriented non-centrosymmetric particles.[18–25] All these previous studies have demonstrated mainly the limitations of glass ceramics as non linear optical materials, since both linear and non linear optical properties are not sufficient yet to be used in applications. The replacement of a single crystal optical element by a glass ceramic with nonlinear optical properties demands currently the improvement of two key parameters: i) the optical transparency, which is determined mainly by the dispersion of refractive index between glass and crystallites, and ii) the crystallite orientation within the bulk of the glass matrix to permit a coherent non linear optical response from all the assembly of crystallites.

We have reported recently the development of lithium niobate-silicate glass ceramics with strong SHG response in the bulk.[15] In the present work we employ multiscale characterization techniques to understand the origin of the unusual bulk SHG signal in such advanced glass ceramic materials. In particular,

H. Vigouroux, Prof. E. Fargin, S. Gomez
CNRS, Université de Bordeaux
Institut de Chimie de la Matière
Condensée de Bordeaux
87, avenue du Dr. A. Schweitzer, 33608
Pessac Cedex, France
E-mail: fargin@icmcb-bordeaux.cnrs.fr
Dr. B. Le. Garrec
CEA-CESTA
15 avenue des Sablières, 33114 Le Barp, France
Dr. G. Mountrichas, Dr. E. Kamitsos
Theoretical and Physical Chemistry Institute
National Hellenic Research Foundation
48 Vassileos Constantinou Ave., 116 35 Athens, Greece
F. Adamietz, Dr. M. Dussauze, Prof. V. Rodriguez
Université de Bordeaux
Institut des Sciences Moléculaires–CNRS UMR 5255
351 cours de la Libération, 33405 Talence Cedex, France
E-mail: v.rodriguez@ism.u-bordeaux1.fr

DOI: 10.1002/adfm.201200651

both the far field response of the material and the individual response from the crystallites are addressed. At first we focus on defining a reproducible, easy and fast process to develop this glass-ceramic material, as well as key parameters for improving its transparency. Then an original multi-scale approach is proposed: i) coupled microscopic techniques, μ-Raman and μ-SHG, have been used to study the isolated crystallites, their nature, shape and the typical size of the nonlinear active crystallites; ii) far-field techniques including small-angle harmonic light scattering (SAHLS) to cross-check the typical size of the nonlinear active crystallites and polarized SHG measurements to control the SHG efficiency of the glass-ceramic and its isotropic nature. The challenge with such coupled analysis is to propose a mechanism at the origin of the observed strong bulk SHG signal.[15]

2. Results and Discussion

2.1. Glass-Ceramic Synthesis

Glasses with composition $35Li_2O$-$25Nb_2O_5$-$40SiO_2$ (called LNS 25) were prepared using Li_2CO_3, (Merck, 99%), Nb_2O_5 (Alfa Aesar 99.9%) and SiO_2 (Alfa Aesar, 99.8%). All batches (~20 g) were prepared by a conventional melt-quenching method. Melting of oxides in respect to glass stoichiometry was performed at ambient atmosphere in a platinum crucible at 1450°C for 30 min. The melts were poured on a stainless steel plate at room temperature and pressed by another plate to obtain samples with a thickness of approximately 1 to 1.5 mm. The glasses were annealed for 15 h at 510 °C (70 °C below the glass transition temperature) to remove internal stresses, and then were slowly cooled to room temperature at a cooling rate of 1 °C/min. Glasses were cut in shape (0.8 to 1.8 mm thickness slices) and polished on both faces for optical quality.

Glass-ceramic samples were prepared in a two step heat treatment performed under air atmosphere on polished glasses: LNS25_a was heat treated for 1 h at 620 °C followed by a growth step at 690 °C for 75 min,[15] and LNS25_b which was heat treated for 2 h at 580 °C for the nucleation step and 17 min at 670 °C for the growth step. After these treatments, an additional polishing step on both sides was carried out on some samples to remove different surface layer thicknesses (45 to 605 μm on both sides of the sample). Note that LNS25_b1, LNS25_b2 and LNS25_b3 glass-ceramic samples were obtained under the same thermal conditions. The main characteristics of these samples are gathered in **Table 1**.

Table 1. Characteristics of the developed and studied glass-ceramic samples.

Sample	Treatment *nucleation*/ growth	Initial thickness [μm]	Final thickness for optical characterizations [μm]
LNS25_a	*620 °C 1 h*/690 °C 75 min	850	760
LNS25_b1	*580 °C 2 h*/670 °C 17 min	1650	1650
LNS25_b2	*580 °C 2 h*/670 °C 17 min	1700	900
LNS25_b3	*580 °C 2 h*/670 °C 17 min	1650	440

2.2. Optical and Structural Characterizations

2.2.1. Optical Transmission

Transmission spectra of the developed glass ceramics as well as of the as-quenched glass have been measured and are reported in **Figure 1**a.

The refractive index has been measured at 935 nm for the as-quenched glass and is n = 1.85 ± 0.01. This high refractive index is likely due to the high niobium concentration,[26–28] and explains partially the medium transmission value (not corrected from multi reflection effects) of the as-quenched glass in the near-IR range (T = 82% at 1064 nm).[15] Residual internal scattering occurring in the as-quenched glass may explain the additional transmission loss. Currently, in comparison to glass-ceramic samples, the as-quenched glass is expected to give the best optical transmission.

In Figure 1b we have reported the transmission at 1064 nm as a function of sample thickness for the LNS25_b series. Each glass-ceramic sample is found to exhibit lower transmission than the initial as-quenched glass. The loss of transmission increases with sample thickness, giving relative loss-values less than 1% for the thinner sample LNS25_b3, 11% for LNS25_b2 and 45% for the thicker sample LNS25_b1. Note also that the increase of scattering losses is strongly correlated with the increase of duration and temperature of the growth heat-treatment. These two parameters are expected to favor drastically crystallization, as illustrated by the LNS25_a sample where a relative transmission loss of 60% occurs at 1064 nm for only a thickness of 760 μm.

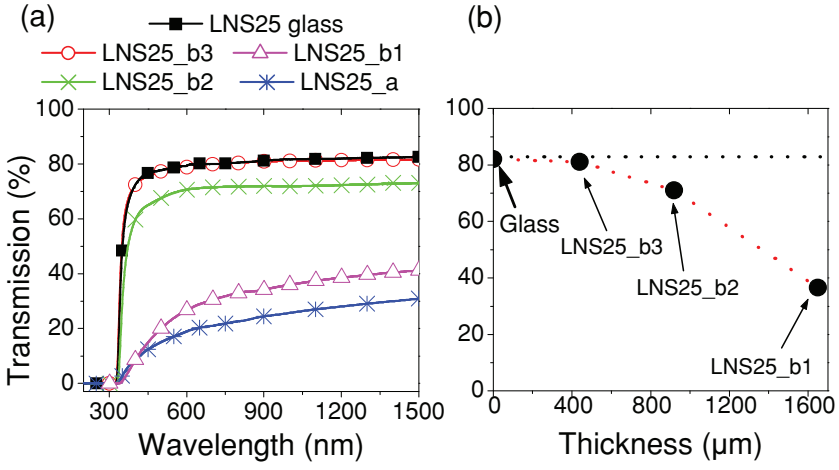

Figure 1. Transmission spectra of LNS25_a, LNS25_b1, LNS25_b2, and LNS25_b3 glass-ceramics and of the as-quenched glass (a), and transmission at 1064 nm as a function of thickness for the LNS25_b glass-ceramic samples (b). The thickness for the glass-ceramic samples is given in Table 1 and for the as-quenched glass LNS25 is 1500 μm.

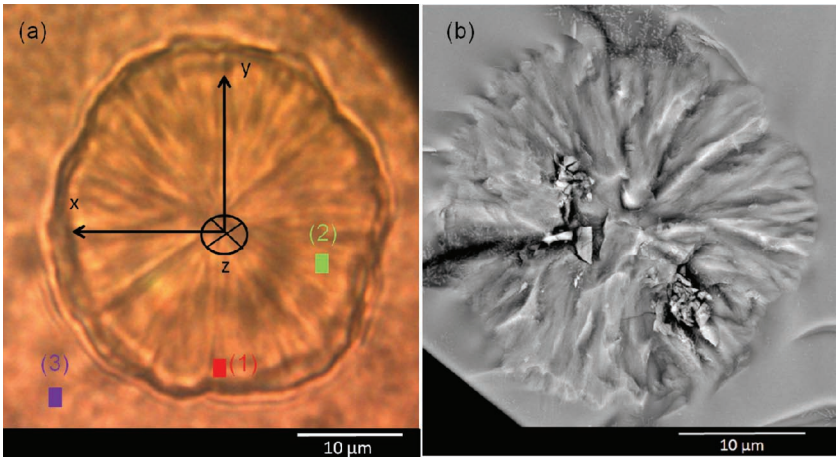

Figure 2. Typical spherulite of LNS25_a glass-ceramic sample a) observed through an optical microscope in the transmission mode and b) a high-resolution environmental SEM. The xyz axes represent the arbitrary orthogonal lab-framework. Points 1, 2, and 3 symbolize different areas where further analyses were carried out.

2.2.2. Optical and Electronic Microcopies

Optical microscopy performed in the transmission mode has been carried out on both glass-ceramic series. For all samples a statistical distribution of spherulite domains with a diameter ranging from 25 to 35 µm was observed. These heterogeneities are probably at the origin of most additional transmission losses observed in the previous section, since Mie scattering is expected to occur because of the large heterogeneity sizes with respect to the wavelength of light. Microscopy clearly evidenced that the spherulite number density is larger in LNS25_a than in LNS25_b glass-ceramics, thus confirming that longer growth duration and higher temperature of treatment increase the number of spherulites. Considering the LNS25_b series, the number density of spherulites is evaluated comparable and homogeneous in LNS25_b1 and LNS25_b2 both samples containing more spherulites than LNS25_b3. The latter sample has been strongly polished on both sides, pointing out a scarcity of spherulites when moving away from the sides of the plate and toward the core of the glass-ceramic material.

Focusing now on a typical spherulite by optical microscopy (**Figure 2**a), we observe contrasted line shapes which are radially distributed. On the other hand, ESEM microscopy images obtained on a bulk crystallized sample reveal also inhomogeneities which are rather radially distributed inside the ca. 30 µm spherulite (Figure 2b). While spherulitic growth is usually observed in organic polymeric materials,[29,30] similar crystallization growth behavior has been reported also for inorganic glass materials like apatite-mullite glass ceramics,[31,32] blast furnace slag glass,[33] lithium disilicate glass ceramic,[34,35] $LaBGeO_5$ glass[36] and the $LiBO_2$-Nb_2O_5 glassy matrix.[37] In particular, Prasad et al.[37] studied the crystallization of the 85LiBO2-15Nb_2O_5 glass composition and observed spherulites in the size range 20–30 µm, including $LiNbO_3$ crystallites of ~25 nm in size. They attributed the spherulite formation to phase separation followed by a coalescence process on further heating.

We note that in the bulk of LNS25 glass-ceramics only spherulitic domains of 25 to 35 µm have been observed. In contrast, smaller spherulites (1–4 µm) crystallize at the surface but with a higher number density probably because of a larger nuclei precipitation. By going deeper into the glass-ceramic bulk, a reduced amount of nuclei can precipitate and particles can then grow up by limited diffusion process[32] as supposed in these LNS25 glass-ceramic materials.[15]

2.2.3. Polarized Micro-Raman Spectroscopy

Polarized micro-Raman spectroscopy was performed on different areas of the LNS25_a sample (Figure 2a), with areas 1 and 2 (3) located inside (outside) the spherulites structure. They have been carried out with the oriented polarization along the y-axis of the lab-framework (VV), for both incident and analyzed configurations (Figure 2a). The Raman spectrum (**Figure 3**a) of area 3 contains a main band centered at ca. 810 cm^{-1}, attributed to Nb-O stretching modes of distorted NbO_6 octahedra sharing at least one corner with SiO_4 tetrahedra,[26–28,38,39] and hence characteristic of the LNS25 glass. Looking at the polarized Raman spectra recorded in two different zones of the same spherulite, we observe essentially the same spectral features with relative intensity modifications. The peak centered at 620 cm^{-1} is assigned to the stretching mode of NbO_6 octahedra

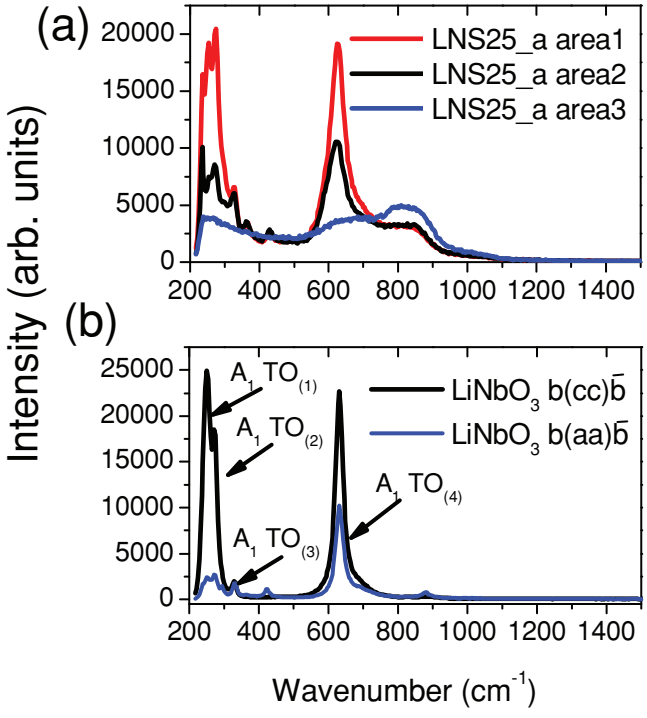

Figure 3. a) Polarized Raman spectra (VV) of the glass-ceramic LNS25_a measured at different areas of the spherulite (area 1, area 2 and area 3 in Figure 2) and b) polarized Raman (VV) spectra of $LiNbO_3$ crystal "b-cut" in $b(cc)\bar{b}$ and $b(aa)\bar{b}$ backscattering geometries following Porto's notation.[45]

Table 2. Raman results of a b-cut $LiNbO_3$ single-crystal and assignments according to literature.[40–44]

This study [cm^{-1}]	Claus et al.[40] [cm^{-1}]	Assignment
250	255	$A_1(TO_{[1]})$
275	276	$A_1(TO_{[2]})$
329	333	$A_1(TO_{[3]})$
631	633	$A_1(TO_{[4]})$

within a 3D niobate network formation,[26–28] and corresponds to a phonon in the $LiNbO_3$ crystalline phase.[40–44] The measured peak at 620 cm^{-1} is however not as sharp as observed in $LiNbO_3$ crystal (Figure 3b), but this broadening could be explained by the non-stoichiometric Nb/Li ratio in the $LiNbO_3$ crystallites.[42]

The crystallites orientation inside the spherulite is expected to modify the relative intensity of Raman bands recorded in the spherulite, and thus it can be revealed by considering the polarized Raman spectra of the $LiNbO_3$ crystal. One simple way to quantify the anisotropy of the crystal is to compare the Raman spectra of a *b*-cut $LiNbO_3$ single-crystal measured with polarizations parallel and perpendicular to the *c-axis* direction. Following Porto's notation,[45] when the Raman excitation and polarization fields are parallel to the crystal *c*-axis and the beam propagates along the b direction ($b(cc)\bar{b}$), we expect only the A_1 TO modes. The $b(aa)\bar{b}$ geometry, where the Raman excitation and polarization fields are now along the *a*-axis direction, will give both the A_1 TO and E TO modes. The measured polarized Raman spectra of $LiNbO_3$ crystal are given in Figure 3b, while the frequencies of characteristic bands with proposed assignments[40–44] are gathered in **Table 2**.

We focus only on the A_1 TO modes that could be mostly observed in the Raman spectra measured with $b(aa)\bar{b}$ geometry, probably because of the very weak E mode intensity. In the $b(cc)\bar{b}$ geometry, we observe two sharp bands at 250 cm^{-1} and 275 cm^{-1} that give a strong peak in the low frequency range, which is nearly extinct in the $b(aa)\bar{b}$ geometry. Therefore, these two bands can be used as sensitive probes of crystal orientation when compared to the high frequency mode at 631 cm^{-1} (Figure 3b). Looking back now at the Raman spectra of the LNS25_a glass-ceramic (Figure 3a), the relative intensity of the band envelope ranging from 200 to 300 cm^{-1} is maximum in area 1, which is radially parallel to the excitation/polarization direction, and is greatly reduced in area 2 which is radially perpendicular to the excitation/polarization direction. This strong intensity variation reveals a sharp radial *c*-axis orientation of $LiNbO_3$ crystallites inside the spherulite. Needle-shaped crystallites are thus expected to fulfill such a radial and rather sharp distribution. In contrast, the Raman spectrum recorded in area 3 (outside the spherulite) does not reveal any level of crystallization and is quite typical of the initial as-quenched glassy material.

2.2.4. Combined Polarized Raman and SHG mapping

In order to assess the distribution and orientation of the $LiNbO_3$ crystallite inside the spherulite, polarized Raman maps have been obtained by selecting the 250 cm^{-1} band which is a good probing technique to detect the orientation of $LiNbO_3$ crystallites as discussed vide supra. **Figure 4**a–d report the Raman maps (step 1 µm, objective 100×) obtained at different angles of parallel polarizations with respect to an initial arbitrary orientation relatively to the y-axis, namely 0, 30, 60 and 90° respectively. As expected from Figure 3a when selecting a spectral domain around 250 cm^{-1}, a constant intensity close to the noise level (blue) clearly maps the glassy matrix outside the spherulite area. However, crystallites inside the spherulite with their *c*-axis distributed around the polarization direction give an irregular but strong Raman signal over a solid angle of ~45° that rotates with the excitation direction from 0 to 90° (see Figure 4a–d). This result is consistent with a radial distribution of $LiNbO_3$ crystallites where the *c*-axis is oriented up or down along the radius of the spherulite, in accordance with other spherulite crystallization habits.[34–36]

SHG maps (step 1 µm, objective 100×) of the same spherulite undertaken at the same polarization angles are reported in Figures 4e-h. The features observed in the SHG maps are identical to those observed in Raman where the signal covers a solid angle of ~45° that rotates with the excitation direction from 0 to 90°. $LiNbO_3$ is a SHG-active structure with one strong and dominating d_{33} non linear coefficient. Hence, maps registered at the same polarization angle point out a perfect correlation with the Raman measurements and indicate now that only $LiNbO_3$ crystallites with *c*-axis parallel to the polarization direction give sharp local SHG signal. In particular, because SHG is a coherent technique which is dipolar sensitive, this result is consistent with a radial distribution of $LiNbO_3$ crystallites where all the *c*-axes are oriented either up or down along the radius of the spherulite to result in a macroscopic polar radial distribution of the $LiNbO_3$ crystallites. Some SHG intensity inhomogeneities can be observed as in the Raman maps, but at a greater extent because SHG is a two-photon excitation process. These intensity defects are probably due to i) a non-perfect radial homogeneous distribution and/or ii) a more or less loss of polarization due to scattering domains encountered by the input and output beams.

2.2.5. Size and Shape of $LiNbO_3$ Crystalline Particles

We have previously demonstrated by µ-Raman spectroscopy that the $LiNbO_3$ crystallites are located and radially oriented inside the spherulites. In this section we aim to characterize the sizes of these crystallites, which are supposed to be needle-shaped with two very different size scales that cannot be simply estimated with the same technique. From X-ray diffraction results reported in our previous study,[15] the smaller dimension of $LiNbO_3$ crystallite has been estimated in the range of 35 to 45 nm in the LNS25_a glass-ceramic sample. The larger dimension of the crystalline particles has been assessed by two far field complementary nonlinear optical techniques: small angle harmonic light scattering (SAHLS) and high resolution SHG mapping.

The SAHLS technique is a very powerful technique that selectively allows to measure wavelength-sized materials/particles that are SHG active, i.e. here the $LiNbO_3$ crystallites. The second harmonic signal of the plate (set at fixed normal incidence) has been measured, using an excitation line at 1064

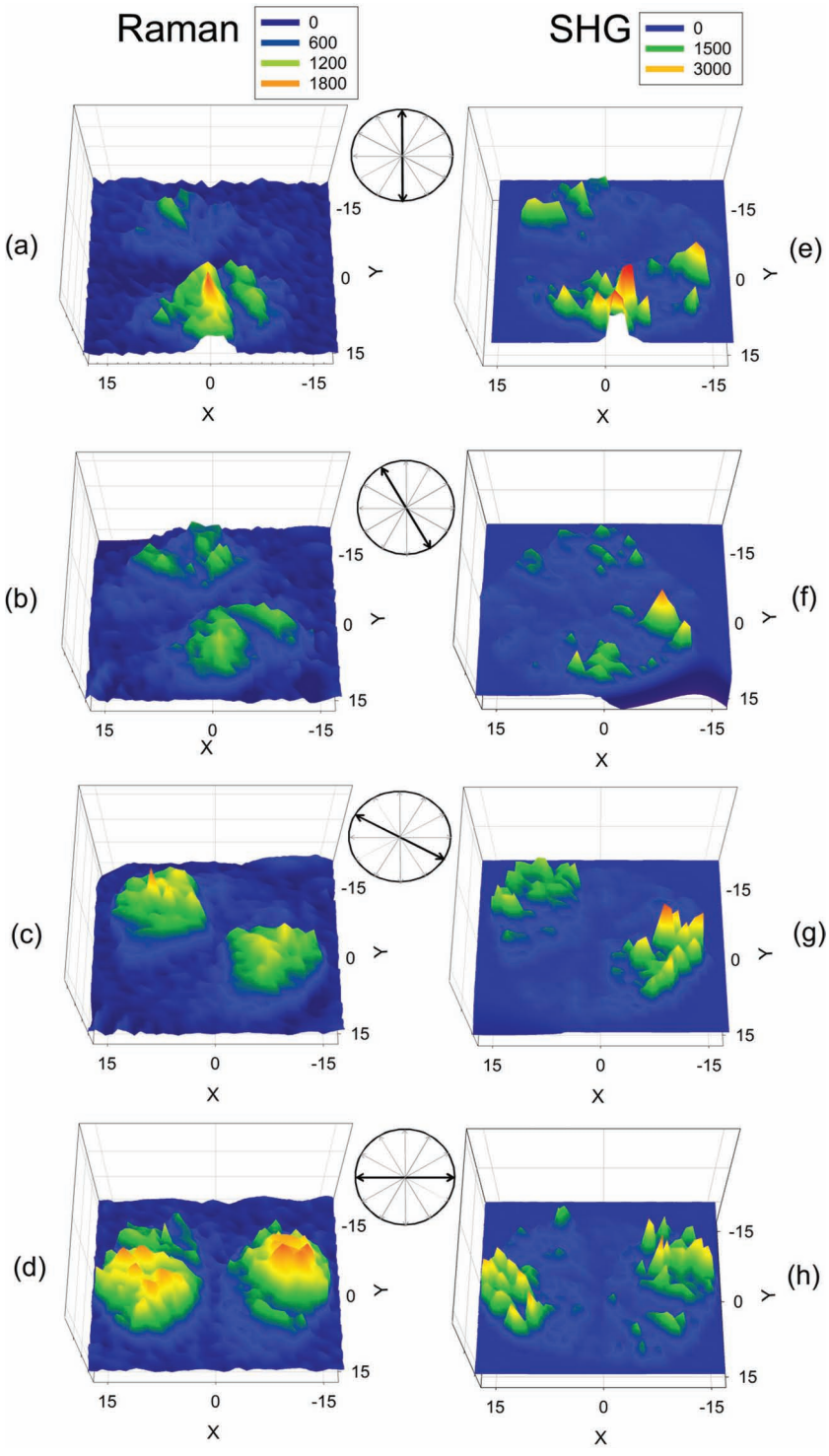

Figure 4. Probing a spherulite of LNS25_a glass ceramic: Raman mapping at different angles of polarization (0, 30, 60, 90°) (left) and micro-SHG mapping at the same angle of polarizations (right). Both mapping scales are expressed in µm along X and Y directions.

nm, as a function of the angular transfer moment, specified by the angle θ between the rotating detector and the forward transmitted beam (**Figure 5**a). The SAHLS signal is detected in a narrow angular sector close to the forward transmission direction. The radius of gyration corresponding to the largest dimension of the crystallites has been obtained using the Guinier approximation, assuming a homogeneous distribution:

$$I_{(Q)} = I_0 \times \exp\left[-(\hat{r}\,Q)^2/3\right] \quad (1)$$

where I_0 is the forward intensity (at θ = 0), $\hat{r}$ the radius of gyration of the nonlinear optical scattering crystallites and the transfer of moment Q is given by $Q = 4\pi\sin(\theta)/\lambda$, with θ the angle between the detection direction and the forward scattered light, and λ the wavelength. The best fit of the experimental results to Equation 1 is reported in Figure 5b with a radius of gyration $\hat{r} = 760 \pm 20$ nm.

To confirm the above results for the radius of gyration, a high resolution SHG mapping with a 0.2 µm step has been carried out. This selective NLO imaging technique revealed typical hot SHG spots of 600 to 800 nm inside the spherulites (**Figure 6**). In accordance with the SAHLS results, high resolution SHG mapping confirmed the presence of SHG-active crystals with larger size around 700 nm, which are identified to the $LiNbO_3$ crystallites demonstrated by µ-Raman experiments.

Complementary SEM images recorded at the surface of a LNS25 glass-ceramic heat-treated at temperature around T_g showed dispersed needle-like crystallites of 1–2 µm with an anisotropic ratio ca. 2 to 5. $LiNbO_3$ has a hexagonal structure where [001] is a dense atomic packing plane[46] whose perpendicular direction, i.e along the *c*-axis, is supposed to match the crystal growth direction. In contrast to crystal growth at the surface, additional orientational/constraints processes are necessary to reach the radial distribution of oriented crystallites inside spherulites with 20–30 µm diameters.

First, an obvious difference does not concern the larger dimension but rather the cross-section, whose size does not range hundreds of nm but rather tens of nm. We assume that inside the spherulite the crystal growth perpendicularly to the *c*-axis is less efficient probably due to the elastic constraints during the crystallization process. This sub-micro needle-like $LiNbO_3$ crystal is SHG-active with a strong 1D d_{33} nonlinear coefficient[47] and with a coherence length of 8–10 µm.[48] Since the crystallites size along the c-axis is ca. 700 nm, no efficient phase matching of SHG conversion is expected.

Second, since the radius of the spherulite is one order of magnitude larger than the typical largest size of the crystallites, a possible multiscale scheme considers a crystallization process giving rather homogenous crystallites with 35–45 nm cross-section and micrometric length regularly

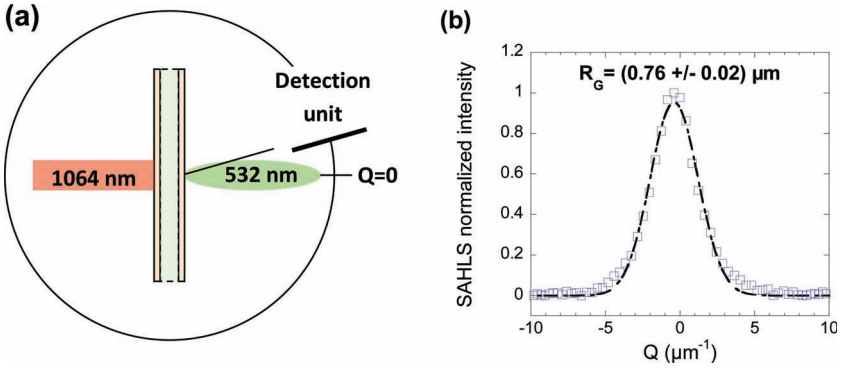

Figure 5. a) SAHLS experimental scheme and b) SAHLS best fit (dotted line) to the experimental curve (square) using Equation (1).

distributed along the radius of a spherulite. The distribution of crystallites is such that they constitute a macroscopic 10–15 µm c-axis oriented poly-crystallite, with consecutive domains spatially radiating incoherent (with no phase relation) SHG signal. To explain the bulk second order optical response of LNS25 glass-ceramic, other macroscopic nonlinear techniques are necessary to probe a larger scale where dispersed spherulites inside a glassy matrix have to be considered.

2.3. Interpretation of the SHG Macroscopic Response

2.3.1. Statistical Macroscopic SHG Response

Macroscopic NLO studies have been performed on the LNS25_b glass-ceramics series because they exhibit the best optical transmission in the visible-near IR spectral range (Figure 1). The NLO studies have been performed using a large collimated beam with diameter 3200 µm as previously detailed[15] in order to probe a large volume of matter to maximize the number of dispersed spherulites and improve the statistics of the detected signal. SHG measurements in transmission at normal incidence have been performed using the continuous polarization scan technique. In contrast to Kurtz and Perry crystalline powder observations,[49] the SHG patterns reported in **Figure 7** are not at all typical of Mie scattering losses since they would give a unique constant signal whatever the polarization state of the incident beam.

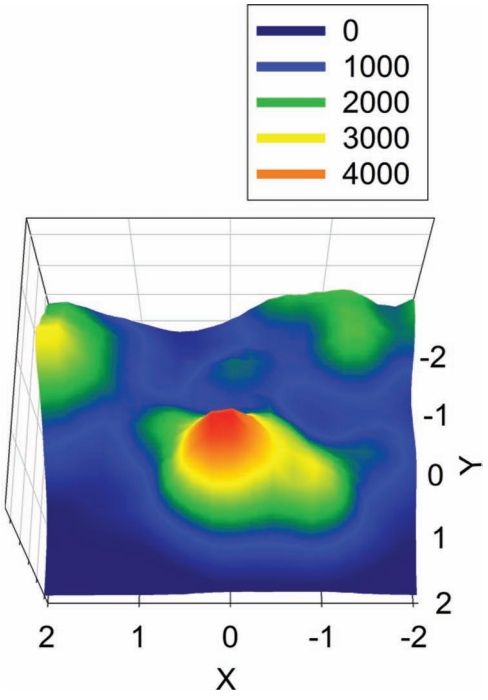

Figure 6. High resolution SHG mapping with a 0.2 µm step;. Scales along X and Y directions are in µm. SHG intensity is in arbitrary units.

As shown in Figure 7, all glass-ceramic samples exhibit a constant background, coming from scattering losses at a level of ~30% of the total signal, which is superimposed to typical polarized signals. In addition, we note that the ψ-p curve is identical to ψ-s but 45° shifted. Unambiguously, this shifted equivalent response indicates that each sample is in-plane isotropic as expected. To asses further the nature of this response, a glass-ceramic sample has been elaborated in the shape of a cube and SHG polarization measurements performed on each face gave the same features. This result confirms definitively the isotropic 3-D nature of the macroscopic nonlinear response of the developed glass-ceramic materials.

According to results in figure 7, the ratio between *pp* and *sp* maximum intensity $r_{pp/sp}$ ranges from 4 to 7 depending on the sample. Thus, the macroscopic SHG response seems to be rather compatible with $LiNbO_3$ needle-like crystallites where a strong one-dimensional d_{33} nonlinear coefficient dominates the nonlinear optical response.[50] Note that a statistical broad distribution of *c*-oriented $LiNbO_3$ needle-like crystallites perpendicular to the surface would give $r_{pp/sp} = 9$.

2.3.2. On the Origin of the Statistical Macroscopic SHG Response

We assume that the spherulites dispersed inside the glassy matrix are at the origin of the SHG macroscopic patterns observed in Figure 7, as well as those reported in reference.[15] According to Kurtz and Perry,[49] there is a typical volume where the second-harmonic fields are phase correlated. Those volumes have size that fits the coherence length l_c. Noteworthy, the spherulites observed in this work are almost spherical objects with diameter D ~ 25–35 µm which is approximately twice the coherence length of the material, l_c ~ 8–10 µm. Hence, the elementary SHG signal radiated from a spherulite can be decomposed in two nearly independent contributions coming from two mirrored elementary volumes, one (V_{left}) with a net polarization pointing toward the left hand-side and the other (V_{right}) with a net polarization pointing toward the right hand-side with respect to the direction of propagation (see **Figure 8**). The twin volumes V_{left} and V_{right} radiate coherently SHG signals with opposite amplitudes.

Indeed, the net SHG signal coming from each spherulite is strongly dependent on the size of the objects. It decreases with the size of the spherulite until it vanishes when the diameter is

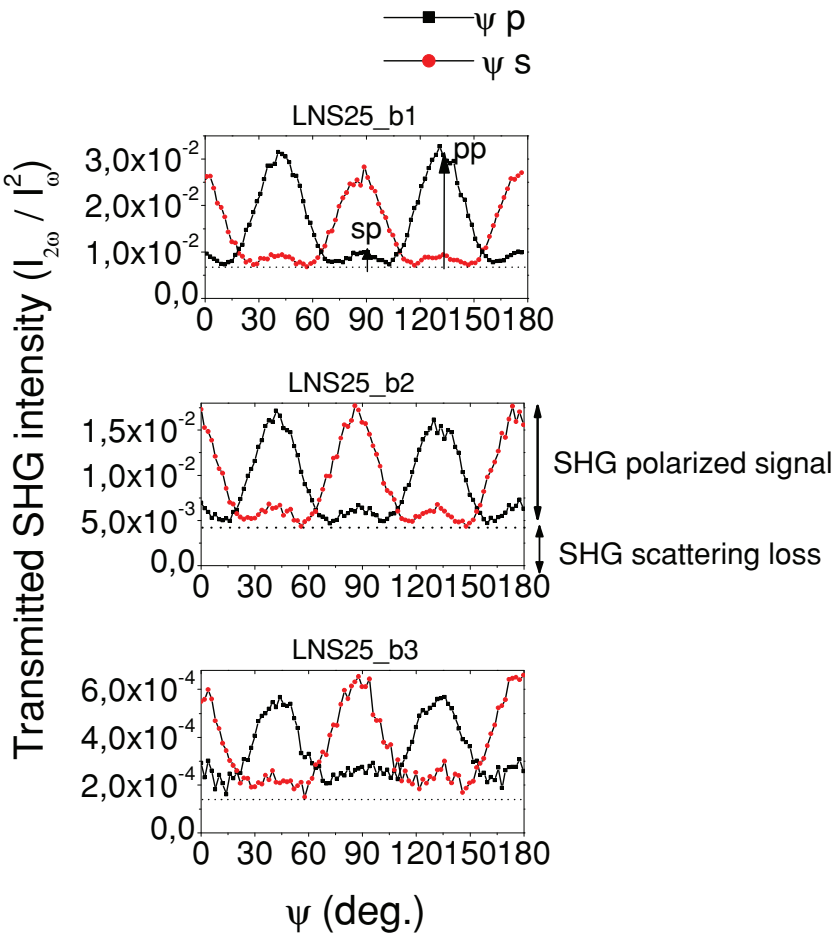

Figure 7. ψ–p (black-square solid line) and ψ–s (red-circle red solid line) scans of LNS25_b1, LNS25_b2 and LNS25_b3 glass-ceramic materials. pp and sp intensities are indicated with arrows and occur periodically at (45, 135°) and (0, 90, 180°), respectively.

less than the wavelength, i.e. local isotropy is reached because all dipolar effects cancel out. However, the spherulite SHG signal is expected to be maximum when the two elementary volumes scale with l_c^3, i.e., the diameter of a spherulite is approximately twice the coherence length. Radiating volumes that exceed l_c^3 introduce strong interference effects that produce an exponentially decrease of the SHG response and also an increase of the transmission loss of the material because of Mie scattering. Despite this effect, since spherulites are sparsely distributed in the matrix with distances greater than the coherence length, they radiate uncorrelated SHG fields and the total second harmonic intensity is just the sum of the individual contributions (incoherent case). Thus, this signal should be classified as hyper-Rayleigh scattering,[51] but since it comes from large scaled sparse scatterers inside a material, the overall signal is strongly modified by Fresnel transmission factors. In addition, the dipolar/octupolar origin of the NLO signal, which reflects the statistical radial dipolar distribution inside the spherulites, is estimated by the ratio between *pp* and *sp* SHG maximum intensity $r_{pp/sp}$ which ranges from 4 to 7 as found in section 4.1.

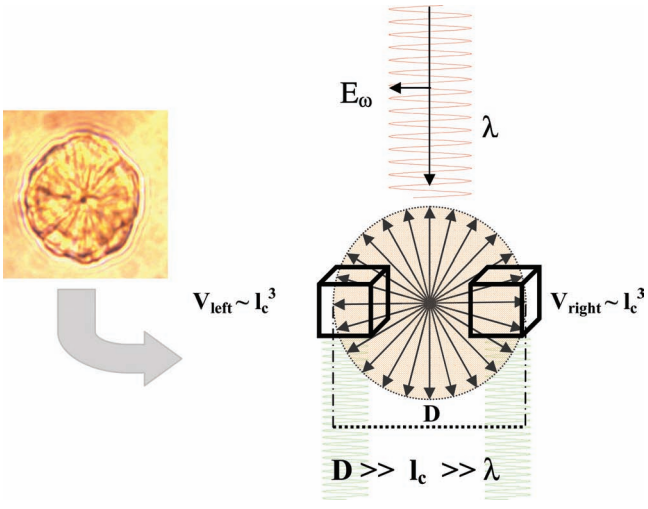

Figure 8. A spherulite as a twin source of SHG signal.

3. Conclusions

We have elaborated advanced glass-ceramic materials with a 3D isotropic SHG response. $LiNbO_3$ crystallites have been founded to grow within spherulite domains with a radial distribution. Correlation between structural and optical properties of the synthesized glass ceramics have been carried out with a multi-scale approach from the sub-micro to the millimeter level. An interpretation of this particular isotropic SHG property has been proposed. Finally, this work has demonstrated i) the great possibility to obtain optical materials with isotropic nonlinear optical response which is unique and of a great interest for applications and ii) key parameters within the glass-ceramic microstructure the manipulation of which can improve further its optical properties.

4. Experimental Section

Structural Characterizations: The crystalline particles in the glass-ceramic samples were recorded using a high resolution environmental scanning electronic microscopy FEI QUANTA 200 ESEM FEG operating at 15 kV, and an optical microscope in transmission mode. These enable the study of the sub-microscopic (hundred of nanometer) and microscopic scale respectively. No preliminary steps were required to observe those samples.

Linear Optical Characterizations: Optical transmission spectra were recorded at room temperature using a double-beam spectrophotometer (CARY, UV-VIS-NIR) in the wavelength range 200–1500 nm. Linear refractive indices at 932 nm and 532 nm were obtained using the Brewster angle reflection method over the +/-[10; 70°] wide theta range. The accuracy of the measured refractive index is better than ±0.01.

Nonlinear Optical Analyses: The second harmonic generation signal measurements were performed as previously described.[15,52] The fundamental unfocused (collimated) beam with a diameter of ~3200 μm at 1550 nm, initially polarized out of the incidence plane (s), is passed through a combination of a rotating half wave plate and a fixed quarter wave plate (vertical fast axis) to address all possible polarizations, from linear to elliptical and to circular polarization. The incident beam is focused on the sample at a fixed incident angle and the transmitted second harmonic light is resolved into components polarized parallel (p) and perpendicular (s) to the horizontal plane of incidence. The second-harmonic intensity is recorded versus the rotation angle of the half-wave plate (angle denoted by ψ). Hence, polarizations scans as a function of the half-wave plate angle ψ have been performed at a fixed incidence angle of 0°. More details about this procedure can be found elsewhere.[53]

μ-Raman and μ-SHG Mapping: In this study we have used a combination of i) μ-Raman scattering spectroscopy and ii) μ-SHG in the reflection mode, employing the same setup to get a direct link between physical properties and local structure. The experimental set up was based on a modified μ-Raman (HR 800, Horiba/Jobin-Yvon) instrument equipped with two laser sources: a picosecond laser at 1064 nm for SHG measurement and a CW laser at 532 nm for Raman excitation. Confocal microscopy and motorized stages (X,Y,Z) allow the 3D imaging of both Raman and SHG signals. The μ-Raman spectra were recorded with a typical spectral resolution of 2.5 cm^{-1} in the backscattering geometry at room temperature. More details about the μ-spectrometer setup and its ability are given elsewhere.[26,54]

Acknowledgements

This work was supported by Région Aquitaine (Advanced Materials in Aquitaine - LasINOF) and by the EU through the Marie Curie Actions–NANONLO project (MTKD-CT-2006-042301). F.A., M.D., and V.R. thank Région Aquitaine for additional financial support in optical, laser, and computer equipment. The authors are grateful to J. Ravaux and R. Podor from Institut de Chimie Séparative Marcoule (ICSM) for the High Resolution Environmental SEM images performed on glass-ceramic samples.

Received: March 8, 2012
Published online: June 4, 2012

[1] G. Peterson, A. Ballman, P. Lenzo, M. Bridenbaugh, *Appl. Phys. Lett.* **1964**, *5*, 62.
[2] E. Spencer, P. Lenzo, K. Nassau, *Appl. Phys. Lett.* **1965**, *7*, 67.
[3] G. A. Smolenskii, N. N. Krainik, N. P. Khuchua, V. V. Zhdanova, I. E. Mylinkova, *Phys. Status Solidi b* **1966**, *13*, 309.
[4] C. Abrahams, J. M. Redy, J. L. Bernstein, *J. Phys. Chem. Solids* **1966**, *27*, 997.
[5] M. M Abouelleil, F. J. Leonberger, *J. Am. Ceram. Soc.* **1989**, *72*, 1311.
[6] T. Honma, Y. Benino, T. Fujiwara, T. Komatsu, *Appl. Phys. Lett.* **2006**, *88*, 231105.
[7] R. Ihara, T. Honma, Y. Benino, T. Fujiwara, R. Sato, T. Komatsu, *Solid State Commun.* **2005**, *136*, 273.
[8] J. Gu, Y. Yan, Y. S. Zhao, J. Yao, *Adv. Mater.* **2012**, *24*, 2249.
[9] A. M. Glass, M. E. Lines, K. Nassau, J. W. Shiever, *Appl. Phys. Lett.* **1977**, *31*, 249.
[10] N. M. Layton, J. W. Smith, *J. Am. Ceram. Soc.* **1975**, *58*, 435.
[11] M. Todorovic, L. J. Radonjic, *Ceram. Int.* **1997**, *23*, 55.
[12] K. Gerth, C. Rüssel, R. Keding, P. Schleevoigt, H. Dunken, *Phys. Chem. Glasses* **1999**, *40*, 135.
[13] V. N. Sigaev, N. V. Golubev, I. Z. Usmanova, S. Yu. Stefanovich, P. Pernice, E. Fanelli, A. Aronne, B. Champagnon, V. Califano, D. Vouagner, T. E. Konstantinova, V. A. Glazunova, *Glass Phys. Chem.* **2007**, *33*, 97.
[14] V. N. Sigaev, N. V. Golubev, S. Yu.Stefanovich, T. Komatsu, Y. Benino, P.Pernice, A. Aronne, E. Fanelli, B. Champagnon, V. Califano, D. Vouagner, T. E. Konstantinova, V. A. Glazunova, *J. Non-Cryst. Solids* **2008**, *354*, 873.
[15] H. Vigouroux, E. Fargin, A. Fargues, B. Le Garrec, M. Dussauze, V. Rodriguez, F. Adamietz, G. Mountrichas, I. E. Kamitsos, J. S. Lotarev, V. Sigaev, *J. Am. Ceram. Soc.* **2011**, *94*, 2080.
[16] J. Zarzycki, *Les Verres et l'Etat Vitreux*, (Ed: Masson), Paris **1982**, Ch.1.
[17] P. W. Mc Millan, *Glass-Ceramics*, Academic Press, London **1964**
[18] Y. Takahashi, Y. Benino, T. Fujiwara, T. Komatsu, *J. Appl. Phys.* **2001**, *89*, 5282.
[19] C. A. C Feitosa, V. R. Mastelaro, A. R. Zanatta, A. C. Hernandes, E. D. Zanotto, *Opt. Mater.* **2006**, *28*, 935.
[20] N. Maryama, T. Honma, T. Komatsu, *Opt. Mater.* **2009**, *32*, 35.
[21] H. Masai, S. Tsuji, T. Fujiwara, Y. Benino, T. Komatsu, *J. Non-Cryst. Solids* **2007**, *353*, 2258.
[22] M. Guignard, V. Nazabal, X. H. Zhang, F. Smektala, A. Moréac, S. Pechev, H. Zeghlache, A. Kudlinski, G. Martinelli, Y. Quiquempois, *Opt. Mater.* **2007**, *30*, 338.
[23] C. G. Lin, H. Z. Tao, X. L. Zheng, R. K. Pan, H. C. Zang, X. J. Zhao, *Opt. Lett.* **2009**, *34*, 437.
[24] C. G. Lin, H. Z. Tao, R. K. Pan, X. L. Zheng, G. P. Dong, H. C. Zang, X. J. Zhao, *Chem. Phys. Lett.* **2008**, *460*, 125.
[25] X. L. Zheng, H. Z. Tao, C. G. Lin, S. X. Gu, G. P. Dong, X. J. Zhao, *Opt. Mater.* **2009**, *31*, 1434.
[26] M. Dussauze, E.I. Kamitsos, E. Fargin, V. Rodriguez, *J. Phys. Chem. C* **2007**, *111*, 14560.
[27] M. Dussauze, E. Fargin, A. Malakho, V. Rodriguez, T. Buffeteau, F. Adamietz, *Opt. Mater.* **2006**, *28*, 1417.
[28] T. Cardinal, E. Fargin, G. Le Flem, S. Leboiteux, *J. Non-Cryst. Solids* **1997**, *222*, 228.
[29] K. L. Singfield, G. R. Brown, *Macromolecules* **1995**, *28*, 1290.
[30] J. L. Hutter, J. Bechloefer, *J. Cryst. Growth* **2000**, *217*, 332.
[31] P. Carpenter, M. Campbell, R. Rawlings, P. Rogers, *J. Mater. Sci. Lett.* **1986**, *5*, 1309.
[32] K. T. Stanton, K. P. O'Flynn, S. Kiernan, J. Menuge, R. Hill, *J. Non-Cryst. Solids* **2010**, *356*, 1808.
[33] C. Fredericci, E. D. Zanotto, E. C. Ziemath, *J. Non-Cryst. Solids* **2000**, *273*, 64.
[34] H. R. Fernandes, D. U. Tulyaganov, A. Goel, M. J. Ribeiro, M. J. Pascual, J. M. F. Ferreira, *J. Eur. Ceram. Soc.* **2010**, *30*, 2017.
[35] S. C. Von Clausbruch, M. Scwheiger, W. Höland, V. Rheinberger, *J. Non-Cryst. Solids* **2000**, *263–264*, 388.
[36] P. Gupta, H. Jain, D. B. Williams, O. Kanert, R. Kuechler, *J. Non-Cryst. Solids* **2004**, *349*, 291.
[37] N. S. Prasad, K. B. R. Varma, *J. Non-Cryst. Solids* **2005**, *351*, 1455.
[38] M. P. F. Graca, M. G. Ferreira da Silva, *J. Mater. Sci.* **2007**, *42*, 2543.
[39] M. P. F. Graca, M. G. Ferreira da Silva, A. S. B. Sombra, M.A. Valente, *J. Non-Cryst. Solids* **2007**, *353*, 4390.
[40] R. Claus, G. Borstel G, E. Wiesendanger, L. Z. Steffan, *Z. Naturforsch. A* **1972**, *27*, 1187
[41] R. Claus, G. Borstel G, E. Wiesendanger, L.Z. Steffan, *Phys. Rev. B* **1972**, *6*, 4878.
[42] A Ridah, P Bourson, M. D. Fontana, G Malovichko, *J. Phys: Condens. Matter* **1997**, *9*, 9687.
[43] R. Schaufele, M. Weber, *Phys. Rev.* **1966**, *152*, 705.
[44] Y. Repelin, E. Husson, F. Bennani, C. Proust, *J. Phys. Chem. Solids* **1999**, *60*, 819.
[45] T. C. Damen, S. P. S. Porto, B. Tell, *Phys. Rev.* **1966**, *142*, 570.
[46] R. S. Weis, T. K. Gaylord, *J. Appl. Phys. A* **1985**, *37*, 191.
[47] H. Jain, *Ferroelectrics* **2004**, *306*, 111.

[48] V. G. Dmitriev, G. G. Gurzadyan, D. N. Nikogosyan, in *Handbook of Nonlinear Optical Crystals, Springer Series in Optical Science*, Vol. *64*, (Ed: A. E. Siegman), Springer-Verlag, Berlin, Germany **1990**.
[49] S. K. Kurtz, T. T. Perry, *J. Appl. Phys.* **1968**, *39*, 3798.
[50] S. Brasselet, J. Zyss, *J. Nonlinear Opt. Phys. Mater.* **1996**, *5*, 671.
[51] T. Verbiest, K. Clays, V. Rodriguez, *Second-order nonlinear optical characterizations techniques: An Introduction*, CRC Press, New York **2009**, Ch.2.
[52] V. Rodriguez, C. Sourisseau, *J. Opt. Soc. Am. B* **2002**, *19*, 2650.
[53] V. Rodriguez, *J. Chem. Phys.* **2008**, *128*, 064707/064701.
[54] a) V. Rodriguez, D. Talaga, F. Adamietz, J. L. Bruneel, M. Couzi, *Chem. Phys. Lett.* **2006**, *431*, 190; b) A. Delestre, M. Lahaye, E. Fargin, M. Bellec, A. Royon, L. Canioni, M. Dussauze, F. Adamietz, V. Rodriguez, *Appl. Phys. Lett.* **2010**, *96*, 091908; c) M. Dussauze, V. Rodriguez, A. Lipovskii, M. Petrov, C. Smith, K. Richardson, T. Cardinal, E. Fargin, E. I. Kamitsos, *J. Phys. Chem. C* **2010**, *114*, 12754; d) P. G. Lacroix, T. Hayashi, T. Sugimoto, K. Nakatani, V. Rodriguez, *J. Phys. Chem. C* **2010**, *114*, 21762; e) P. G. Lacroix, M. C. Munoz, A. B. Gaspar, J. A. Real, S. Bonhommeau, V. Rodriguez, K. Nakatani, *J. Mater. Chem.* **2011**, *21*, 15940.